The Journal of Chemical Physics

RESEARCH ARTICLE | SEPTEMBER 15 2026

Deep potential modeling of oxygen adsorption and surface reconstruction on silica

Special Collection: 2026 JCP Emerging Investigators Special Collection

Guan Zhang ; Xinbin Ye ; Shiwei Hu ; Yonghao Zhang ; Tianbai Xiao ; Quanhua Sun ; Yuan Hu

J. Chem. Phys. 165, 114702 (2026)
https://doi.org/10.1063/5.0346578

AIP Publishing

The Journal of Chemical Physics ARTICLE pubs.aip.org/aip/jcp

Deep potential modeling of oxygen adsorption and surface reconstruction on silica

Cite as: J. Chem. Phys. 165, 114702 (2026); doi: 10.1063/5.0346578
Submitted: 4 June 2026 • Accepted: 31 August 2026 •
Published Online: 15 September 2026

Guan Zhang,[1] Xinbin Ye,[2] Shiwei Hu,[1] Yonghao Zhang,[1] Tianbai Xiao,[1] Quanhua Sun,[1] and Yuan Hu[1,a)]

AFFILIATIONS

[1] State Key Laboratory of High Temperature Gas Dynamics, Institute of Mechanics, Chinese Academy of Sciences, Beijing 100190, China
[2] AI Engineering, Advanced Micro-Fabrication Equipment Inc. China (AMEC), Shanghai 201201, China

Note: This paper is part of the 2026 JCP Emerging Investigators Special Collection.
[a)]**Author to whom correspondence should be addressed:** yhu@imech.ac.cn

ABSTRACT

The binding energy of atomic oxygen on silica has remained uncertain for decades. This quantity directly governs catalytic heating during atmospheric re-entry. Classical potentials overestimate it by an order of magnitude ($ReaxFF^{GSI}_{SiO}$: ~31 eV vs experiment: ~3 eV), while first-principles methods cannot reach the scales required for adsorption equilibration. Although neural network potentials bridge this accuracy–efficiency gap, conventional sampling fails to provide training data spanning rare reactive events within collective phase transitions. Here, we train a neural-network potential (HyGSI) using a hybrid enhanced sampling-machine learning framework coupling on-the-fly probability enhanced sampling with deep potential molecular dynamics. HyGSI covers SiO_2 melting, pressure-dependent surface reconstruction, and oxygen adsorption–recombination. The predicted adsorption energy is 2.96 ± 0.15 eV, consistent with the 1991 experimental estimate (3.00 ± 0.31 eV) and an order of magnitude lower than $ReaxFF^{GSI}_{SiO}$ predictions. Furthermore, surface reconstruction reshapes available catalytic sites, coupling structural evolution to reaction chemistry. These findings provide corrected energetics for hypersonic re-entry heat-flux models and validated force fields for semiconductor plasma etching and fusion reactor wall modeling.

I. INTRODUCTION

Gas–surface interactions are central to technologies spanning energy, manufacturing, and transportation. When reactive species strike a solid surface, the outcomes—protection, erosion, functionalization, or healing—depend on molecular-level processes that remain difficult to predict and control. This challenge intensifies under extreme conditions, where surfaces themselves undergo structural transformations that continuously redefine available reaction sites. Among these systems, atomic oxygen adsorption on silica presents a quantifiable discrepancy. The binding energy estimated from experiment (~3 eV) differs from $ReaxFF^{GSI}_{SiO}$ predictions (~31 eV) by an order of magnitude. Among reactive gas–surface systems, atomic oxygen interacting with silica (SiO_2) stands out for both its technological ubiquity and scientific complexity. In semiconductor manufacturing, oxygen radicals drive atomic-layer oxidation and etching of SiO_2 dielectrics, where nanometer-scale precision determines device performance.[1] The same chemistry governs fusion reactor wall conditioning[2] and optical fiber degradation in harsh environments. Spacecraft reentering Earth's atmosphere encounter dissociated oxygen at velocities exceeding 7 km/s; catalytic recombination on silica-based thermal protection tiles releases energy comparable to convective heating, directly threatening vehicle survivability.[3–5] Despite decades of research across these disparate fields, a unified molecular-level understanding remains elusive: how does oxygen interact with silica, and how does this interaction evolve with temperature, pressure, and surface state?

No existing method simultaneously satisfies three requirements: quantum-mechanical accuracy for bond formation and breaking, computational efficiency for phase-transition timescales, and generality across crystalline, amorphous, and molten states with reactive adsorbates. The challenge is compounded by an often-overlooked complexity: at temperatures exceeding 1000 K, silica itself undergoes melting, amorphization, and pressure-dependent

reconstruction, fundamentally redefining the catalytic sites available to incoming oxygen. The surface is not a static stage, rather it is an active participant whose restructuring couples inseparably to adsorption chemistry. Reactive molecular dynamics with empirical force fields have mapped elementary pathways on idealized surfaces,[6–12] yet, depending on the training set and parameterization, may overestimate adsorption energies and have difficulty reproducing pressure-induced surface reconstruction. *Ab initio* molecular dynamics provide chemical accuracy but remain prohibitive for requisite system sizes and timescales. Machine learning potentials bridge this gap, in principle, but their reliability hinges on training data that must capture rare reactive events embedded within collective phase transitions—a bottleneck that current sampling strategies fail to overcome.

The limitations of existing computational methods stem from fundamental challenges at two levels. Although computationally efficient, ReaxFF parameterizations struggle to describe temperature-dependent surface reconstruction and SiO_2 phase transitions. They also fail to capture adsorption energetics under extreme non-equilibrium conditions. Machine learning force fields (MLFFs), particularly deep potential (DP) methods,[13] offer quantum-mechanical accuracy through neural network architectures but face a critical bottleneck: generating comprehensive training datasets. *Ab initio* molecular dynamics (AIMD) simulations scale as $O(N^3)$,[14–19] rendering the microsecond trajectories required for capturing rare reactive events.[20–22] While enhanced sampling techniques, such as on-the-fly probability enhanced sampling (OPES),[23] have accelerated rare-event exploration in biomolecular systems,[24–27]

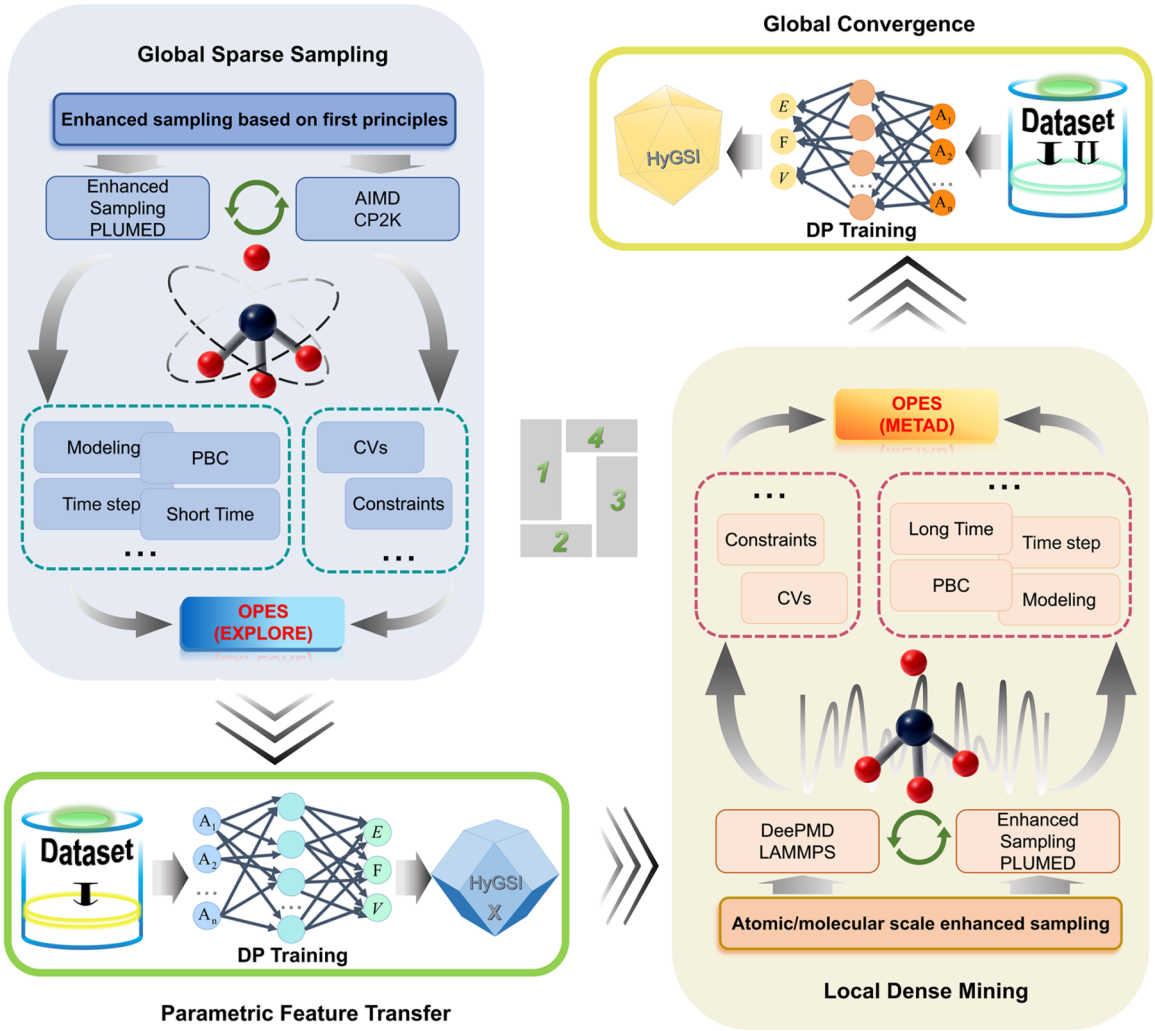

FIG. 1. Hybrid enhanced sampling-machine learning (HES-ML) framework. The four-tier architecture bridges quantum and classical dynamics. Stage I: global sparse sampling using CP2K/PLUMED to generate initial data. Stage II: parametric feature transfer to create the initial potential (HyGSI-X). Stage III: local dense sampling using HyGSI-X to refine the phase space. Stage IV: global convergence training to generate the final HyGSI model.

their application to high-temperature gas–surface reactions remains underdeveloped, facing exploration–convergence trade-offs that can trap simulations in local energy basins.[23]

The oxygen adsorption energy on silica is 2.96 ± 0.15 eV, consistent with experiment and correcting the order-of-magnitude overestimation by the 2013 O/SiO_2 ReaxFF parameterization $ReaxFF^{GSI}_{SiO}$.[28] We obtained this result using HyGSI, a neural-network potential trained through a hybrid enhanced sampling-machine learning (HES-ML) framework that couples OPES-driven configuration sampling with deep potential training. HyGSI covers SiO_2 thermal expansion, pressure-dependent surface reconstruction, and oxygen adsorption–recombination within a single potential. The corrected adsorption energetics provides revised input to heat-flux models for spacecraft thermal protection, where catalytic recombination heating has been modeled using force fields with known systematic errors.

II. COMPUTATIONAL DETAILS

A. HES-ML framework

Integrating deep potential molecular dynamics (DeePMD) with OPES combines quantum-accurate potentials with extensive phase-space sampling. Our HES-ML framework exploits this synergy to model extreme gas–surface interactions. The framework employs a four-tier architecture (Fig. 1) that bridges quantum accuracy and classical computational speed.

Stage I: Global sparse sampling. We utilize OPES-explore in CP2K to perform adaptive enhanced sampling. By optimizing Gaussian kernel widths and free-energy barrier thresholds, we efficiently capture sparse training data (Dataset-I). This approach significantly reduces computational costs compared to well-tempered metadynamics while maintaining sensitivity to rare events.

Stage II: Parametric feature transfer. By projecting atomic environments onto deep feature descriptors, we construct an exploratory potential, HyGSI-X. This baseline model achieves an energy accuracy of <10 meV per atom, serving as a computationally efficient driver to bootstrap the dense phase-space mining in subsequent steps.

Stage III: Local dense mining. We integrate DeePMD into LAMMPS with OPES-metad to perform dense sampling. A notable feature of this stage is sublinear kernel density growth. This enables more efficient sampling of high-energy configurations than conventional AIMD at fixed computational budget.

Stage IV: Global convergence. Finally, we train the model on combined cross-scale datasets (I and II) to generate HyGSI. This potential achieves chemical accuracy across all three regimes (melting, reconstruction, and adsorption). Energy RMSE <3 meV/atom, and force RMSE <200 meV/Angstrom.

B. Dataset generation and potential training

The quality of training datasets determines the transferability of potential functions. We systematically investigated three critical processes relevant to silica thermal protection during re-entry: (i) melting induced by atomic oxygen bombardment, (ii) dynamic surface reconstruction under temperature variations, and (iii) oxygen-induced surface reactions. By applying HES-ML at both AIMD and DeePMD levels, we generated the comprehensive HyGSI potential.

1. Melting dynamics

Simulating SiO_2 melting requires structural descriptors that distinguish crystalline from amorphous phases. We utilized the three-dimensional structure factor (3DSF) to characterize long-range order [Fig. 2(a)]. This metric offers significant advantages over conventional radial distribution functions for tracking crystallization dynamics.[29]

2. Surface reconstruction

We developed a hierarchical approach combining constraint-enhanced AIMD with machine learning potentials to explore the complex landscape of α-quartz (0001) [Fig. 2(b)]. This strategy overcomes a fundamental challenge: sampling high-energy configurations that are thermodynamically relevant but kinetically inaccessible to standard molecular dynamics.

3. Gas–surface reactions

We investigated surface reactions in two pathways: adsorption and recombination. During adsorption, oxygen coordinates at Si–O–Si bridge sites to form metastable trigonal configurations. These evolve into either Si–O–O–Si double-bridges or non-bridging oxygen defects (NBOI) [Fig. 2(c)]. NBOI sites subsequently mediate catalytic recombination [Fig. 2(d)]. These defects are versatile; they can transform into undercoordinated (UC) structures or heal back to pristine surfaces via thermal fluctuations. In the recombination pathway, NBOI sites act as oxygen reservoirs, forming Si–O–O intermediates. Ultimately, NBOI dimerization generates O_2 while leaving paired UC structures.

4. Unified potential

Consolidating these heterogeneous configuration spaces creates a unified training dataset that resolves the exploration–convergence trade-off in OPES sampling. The final HyGSI potential achieves chemical accuracy, with root-mean-square errors of <3 meV per atom for energies and <200 meV $Å^{-1}$ for forces on independent test sets [Figs. 2(e) and 2(f)]. Category-resolved validation against DFT references for melting, reconstructed surfaces, adsorption intermediates, and recombination configurations (Table S3 and Fig. S4 of the supplementary material) confirms this accuracy category by category, with only marginal exceedances, force RMSE up to 214 meV/Å; energy RMSE up to 6.6 meV/atom, the latter dominated by a systematic energy offset in one data subset as detailed in the supplementary material.

C. Enhanced sampling protocols

We implemented a dual-mode On-the-fly Probability Enhanced Sampling (OPES) strategy combining OPES-metad and OPES-explore variants to achieve comprehensive phase-space exploration and accurate free energy convergence.[30,31] In tier I of HES-ML framework, OPES-explore enables extensive sampling across the reaction coordinate space, allowing the discovery of

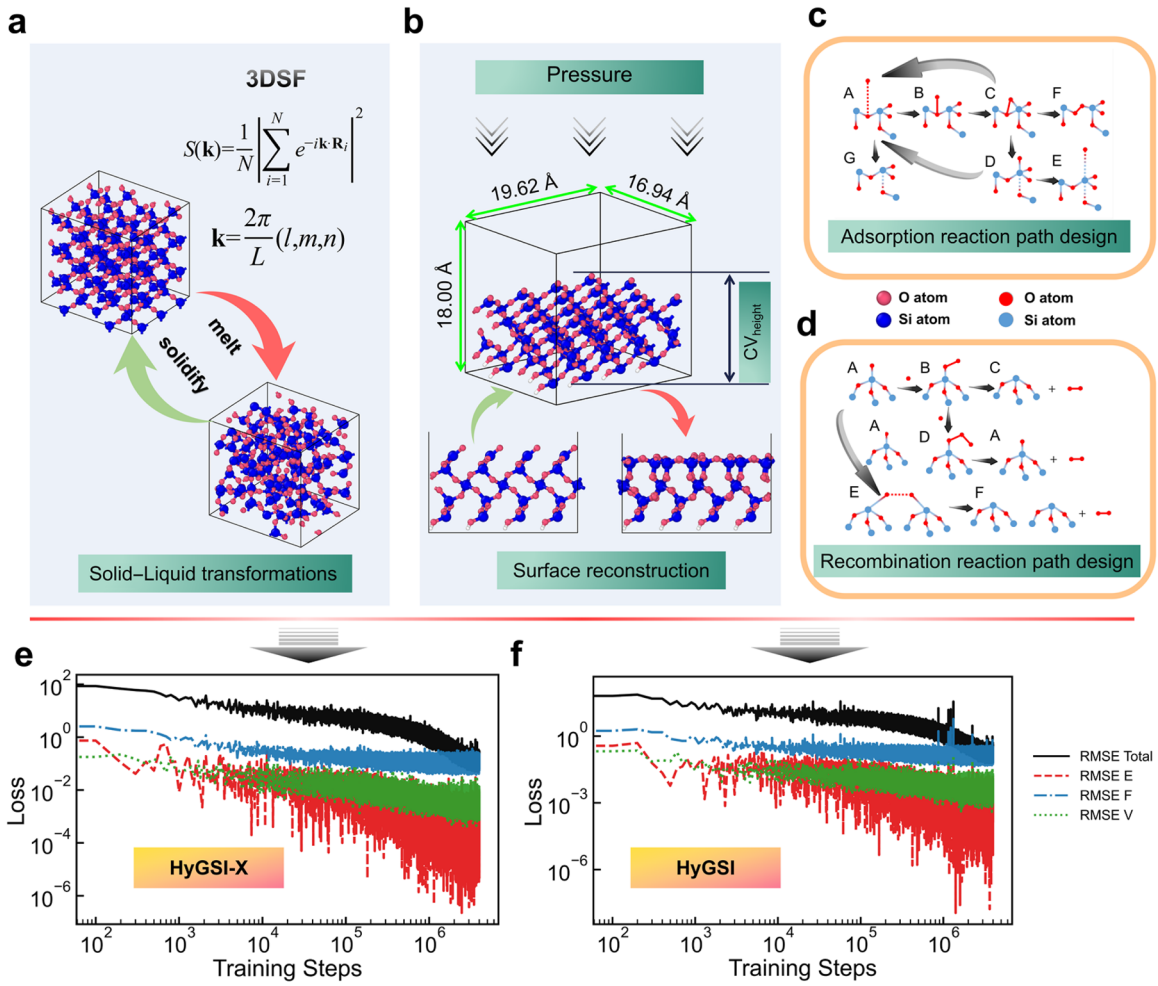

FIG. 2. Hierarchical enhanced sampling strategy and DP training. (a) Three-dimensional structure factor, $S(\mathbf{k})$, characterizes SiO_2 melting and solidification. It preserves crystallographic anisotropy and detects long-range order across phase transitions. (b) Constraint-enhanced sampling of α-quartz (0001) surface reconstruction. Beginning with an unsaturated cleavage surface containing dangling Si and O bonds, the maximum vertical displacement of surface oxygen atoms (CV_{height}) serves as a collective variable to generate diverse reconstruction configurations. (c) Designed reaction pathways for oxygen chemisorption on SiO_2 surfaces. (d) Designed reaction pathways for O_2 catalytic recombination pathways mediated by surface defects. [(e) and (f)] Training convergence for HyGSI-X (e) and HyGSI (f) over 10^6 training steps. HyGSI achieves chemical accuracy (energy RMSE <3 meV per atom; force RMSE <200 meV Å^{-1}) suitable for quantitative predictions of melting, surface reconstruction, adsorption, and recombination reactions.

reaction pathways and surface configurations that are otherwise difficult to access using conventional sampling methods. OPES-metad in tier III provides focused refinement around metastable intermediates, ensuring accurate barrier heights and reaction rates.

The bias potentials were defined as

$$\text{OPES}-\text{metad}\ \ V_n(\mathbf{s}) = \left(1-\frac{1}{\gamma}\right)\frac{1}{\beta}\log\left(\frac{P_n(\mathbf{s})}{Z_n}+\epsilon\right), \quad (1)$$

$$\text{OPES}-\text{explore}\ \ V_n(\mathbf{s}) = (\gamma-1)\frac{1}{\beta}\log\left(\frac{p_n^{\text{WT}}(\mathbf{s})}{Z_n}+\epsilon\right), \quad (2)$$

where $P_n(\mathbf{s})$ is the estimated probability distribution of CVs at the n-th step, computed using Gaussian KDE; ϵ is the regularization term, which limits the maximum bias potential to prevent excessive exploration of high free-energy regions. $p_n^{\text{WT}}(\mathbf{s})$ is the real-time estimated well-tempered sampling distribution, defined as

$$p_n^{\text{WT}}(\mathbf{s}) \propto [P_n(\mathbf{s})]^{\frac{1}{\gamma}}, \quad (3)$$

where the well-tempered distribution flattens $P_n(\mathbf{s})$, enhancing exploration of high-energy regions;

Z_n is the normalization factor, representing the explored volume of CVs space; γ is the bias factor, controlling the broadening

of the target distribution. A larger γ enhances exploration of high-energy regions.

β is the inverse temperature, defined as

$$\beta = \frac{1}{k_B T}, \tag{4}$$

where k_B is the Boltzmann constant and T is the system temperature.

ϵ is the regularization term, which limits the maximum bias potential to prevent excessive exploration of high free-energy regions.

For 3DSF, PLUMED configurations for Dataset-I and Dataset-II share core structural descriptors (ENVIRONMENTSIMILARITY: σ = 0.4, lattice constant = 5.431 Å) with COMBINE-based collective variables constrained by UPPER_WALLS (κ = 1500 kJ/mol, exponent = 3). Dataset-II employed standard OPES-metad (fixed σ = 0.05, PACE = 500, barrier = 2500 kJ/mol) at multiple temperatures for thermodynamic reproducibility. Dataset-I utilizes OPES-explore with adaptive parameters (ADAPTIVE_SIGMA_STRIDE = 100, PACE = 100, barrier = 2000 kJ/mol) at 2000 K for aggressive phase-space sampling.

D. Computational models

Bulk melting simulations utilizing α-cristobalite models contain 324 atoms ($Si_{108}O_{216}$) in cubic cells (15.08 × 17.42 × 16.56 Å^3). Surface processes were investigated using 256-atom slabs ($Si_{80}O_{160}H_{16}$) with the oxygen-terminated surfaces in 19.62 × 16.94 × 18.00 Å^3 cells, with the hydrogen-passivated bottom surfaces. Additional oxygen atoms (1–3) were incorporated for adsorption and catalytic studies, generating $Si_{80}O_{161}H_{16}$, $Si_{80}O_{162}H_{16}$, and $Si_{80}O_{163}H_{16}$ configurations. ReaxFF calculations employed the ReaxFF$^{GSI}_{SiO}$ by Kulkarni *et al.*[28] (derived from the 2003 Si/O set[32]); all comparative statements concerning ReaxFF in this work refer to this specific parameterization, whose known behavior relative to alternative Si/O sets[33,34] is discussed in Sec. III C.

E. DFT and AIMD simulations

First-principles calculations employed CP2K[35] with PBE-D3 functional[36–38] (600 Ry cutoff, 65 Ry rel_cutoff) and DZVP-MOLOPT-SR-GTH basis sets.[39,40] Melting simulations used 3D periodic boundaries with XYZ-periodic Poisson solver, while surface reactions employed 2D periodicity (XY) with Martyna–Tuckermann solver in the non-periodic Z-direction.

AIMD simulations maintained identical parameters but reduced cutoffs (450 Ry, 55 Ry rel_cutoff) for computational efficiency. All simulations used 1.0 fs time steps. Melting employed NPT ensemble (1 atm, CSVR thermostat) at 2000 K for 10 ps without constraints. Surface simulations used NVT ensemble with layer-specific constraints: eight bottom layers were fixed for 2 ps reconstruction studies, while four bottom layers were constrained for 5 ps adsorption/catalysis investigations at 300, 900, and 1500 K, respectively. Static DFT calculations were performed on AIMD-extracted configurations to obtain unperturbed energies, forces, and virials for training data.

III. RESULTS AND DISCUSSION

A. Melting and thermal expansion of α-quartz

As shown in Fig. 3(a), crystalline SiO_2 at low temperatures exhibits two distinct sets of $S(\mathbf{k})$ peaks with comparable heights and spatial positions. To optimize control over the melting process, we assigned weighting coefficients based on the relative peak heights and partitioned them into two independent collective variables, CV_1 and CV_2, as defined by Eqs. (5) and (6): The weights follow a general recipe rather than ad hoc tuning: compute $S(k)$ of the target crystal in the chosen supercell, identify its Bragg peaks, and weight each selected peak by its relative intensity; the specific coefficient values below are, therefore, tied to this supercell and would be re-derived by the same recipe for other cell sizes or polymorphs,

$$CV_1 = 0.35 \cdot S_{\mathbf{k}[3,-2,0]} + 0.35 \cdot S_{\mathbf{k}[3,2,0]} + 0.35 \cdot S_{\mathbf{k}[0,4,0]}, \tag{5}$$

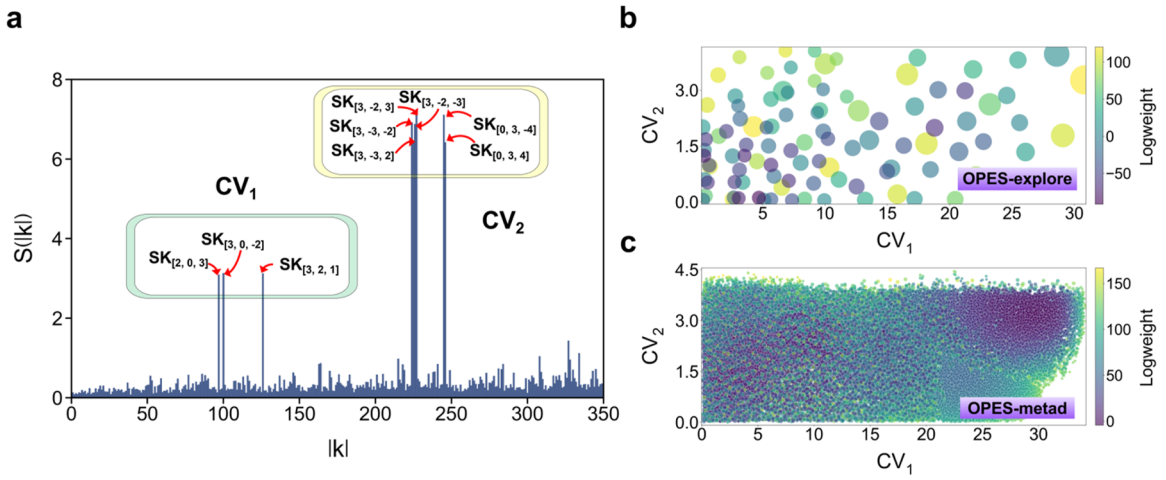

FIG. 3. Sampling of α-quartz melting for DP training. (a) Two collective variables based on three-dimensional structure factor $S(\mathbf{k})$ peaks. [(b) and (c)] Two-level sampling KDE distributions of the α-quartz melting process based on the OPES method: OPES-explore (b) and OPES-metad (c).

$$CV_2 = 0.80 \cdot S_{\mathbf{k}[3,-2,-3]} + 0.65 \cdot S_{\mathbf{k}[3,-2,3]} + 0.7 \cdot S_{\mathbf{k}[3,2,-3]} + 0.75 \cdot S_{\mathbf{k}[3,2,3]} + 0.80 \cdot S_{\mathbf{k}[0,4,-3]} + 0.65 \cdot S_{\mathbf{k}[0,4,3]}. \quad (6)$$

The structural transformation between crystalline and amorphous states was systematically characterized using OPES-enhanced sampling under the NPT ensemble, which enables exploration through coupled variations in CV_1 and CV_2. Figure 3(b) presents the resulting 2D kernel density estimation (KDE) distribution from dataset-I obtained through 2 ps AIMD simulations at 2000 K. While the sampling broadly covers the collective variable space, it exhibits sparsity due to computational constraints. To improve statistical robustness, we supplemented this dataset with additional 1D enhanced sampling along a linear combination of CV_1 and CV_2, ultimately yielding 2000 valid DFT configurations. Figure 3(c) presents the 2D KDE distribution from the dataset-II obtained through 10 ns HyGSI-X MD simulations at 1800, 2000, and 2200 K, respectively. The overlay of these three temperatures through extended timescale simulations enables comprehensive and uniform sampling across the melting region (lower left), solidification region (upper right), and the transition zone between them, effectively avoiding sparsity issues and sampling deficiencies caused by trapping in local minima.

The diverse configurations harvested from the melting sampling serve as the foundational training set for the DeePMD potential, encoding the complex energy landscape of the phase transition. Consequently, characterizing the thermal expansion provides a necessary validation of this potential's transferability, ensuring that the model captures the subtle lattice anharmonicities that drive structural evolution well before melting occurs. While enhanced sampling effectively captures the melting transition between ordered and disordered phases, accurately predicting this phase behavior requires the underlying potential to faithfully reproduce temperature-dependent structural properties of the crystalline phase itself. The melting sampling strategy provides critical structural configurations spanning the solid-liquid transition, but validating potential accuracy necessitates systematic characterization of how crystal structures respond to thermal excitation below the melting point. This crystalline thermal expansion behavior serves as a stringent test: potentials that fail to capture temperature-induced lattice variations will inevitably misrepresent melting thermodynamics and kinetics. Therefore, we proceeded to investigate the thermal evolution of lattice parameters and local structural motifs across a wide temperature range, using the configurations from our enhanced sampling as reference states for assessing potential transferability.

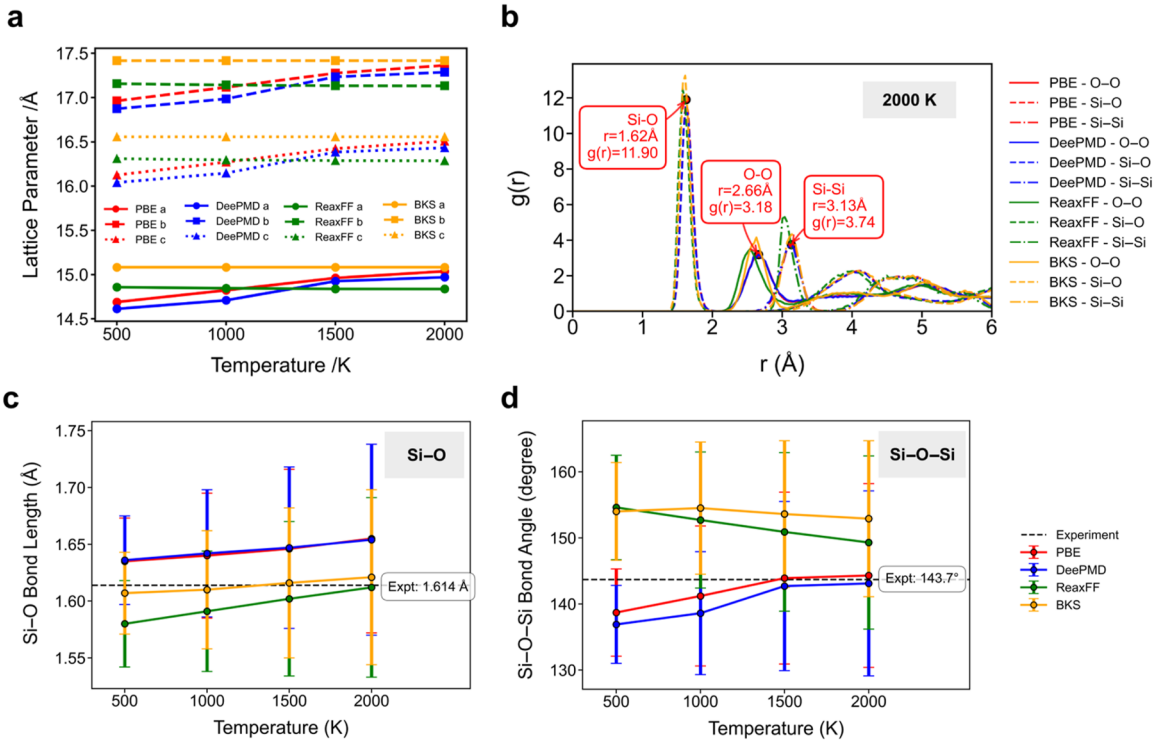

FIG. 4. Thermal evolution and structural analysis of α-quartz. (a) Lattice parameters of a 3 × 3 × 4 supercell from 500 to 2000 K. Comparisons are made between BKS (orange), DeePMD (blue), and ReaxFF$^{GSI}_{SiO}$ (green) potentials against the PBE benchmark (red). (b) Radial distribution functions (RDFs) at 2000 K. [(c) and (d)] Temperature dependence of average Si–O bond lengths (c) and Si–O–Si bond angles (d). The dashed lines indicate experimental values at room temperature; error bars represent standard deviations. DeePMD closely tracks the PBE reference across all temperatures, whereas classical potentials exhibit systematic deviations and minimal thermal response.

Not only does temperature-induced volume expansion in spacecraft thermal protection materials drive bulk cracking but also modulates bond lengths in both bulk and surface structures during oxygen atom catalytic recombination, fundamentally influencing reaction mechanisms. To investigate these critical thermal expansion effects, we tracked the evolution of lattice parameters in a 3 × 3 × 4 α-quartz supercell across temperatures from 500 to 2000 K using NPT ensemble simulations [Fig. 4(a)]. Notably, isothermal MD simulations of intact crystals above the melting temperature generate superheated states, leading to expansion rather than direct melting.

Crystal expansion occurs through combined thermodynamic and entropic effects as thermal energy excites atomic motion, with systems minimizing free energy through structural adaptation. Our comparative analysis reveals differences among various potentials. Both BKS and ReaxFF$^{GSI}_{SiO}$ potentials exhibit negligible thermal expansion-a critical limitation that precludes their use for studying temperature-dependent bulk phenomena. Moreover, these classical potentials display systematic biases: BKS consistently overestimates lattice parameters across the entire temperature range, while ReaxFF$^{GSI}_{SiO}$ shows temperature-dependent errors, overestimating below 1250 K and underestimating above. This behavior suggests that ReaxFF$^{GSI}_{SiO}$ is parameterized to reproduce melting behavior at the expense of thermal transferability. DeePMD shows agreement with PBE reference calculations, with deviations below 0.3 Å throughout the temperature range [Fig. 4(a)].

The quantitative analysis of structural parameters highlights the limitations of classical potentials compared to the accuracy of DeePMD [Figs. 3(c) and 3(d)]. ReaxFF$^{GSI}_{SiO}$ systematically distorts the geometry by underestimating Si–O bond lengths (1.580–1.612 Å) and overestimating Si–O–Si angles (149°–155°), while BKS, despite predicting reasonable bond distances, significantly overestimates angles (153°–154°) and exhibits minimal thermal sensitivity. By contrast, DeePMD faithfully reproduces the PBE results. At 500 K, it yields Si–O bond lengths (1.636 ± 0.039 Å) consistent with the experimental values. At 2000 K, DeePMD captures both systematic bond elongation and enhanced thermal disorder. Standard deviations for bond lengths increase from 0.038 to 0.084 Å, and for angles from ~6° to 14°. The RDFs at 2000 K confirm this agreement with the PBE benchmark. significantly outperforming ReaxFF$^{GSI}_{SiO}$ and BKS in describing high-temperature structures.

DeePMD reproduces first-principles thermal expansion with classical MD efficiency. Thermal expansion has been largely neglected in prior reactive MD studies. The resulting bond-length variation modifies adsorption geometries and lowers reaction barriers at elevated temperatures.

B. Surface reconstruction of α-quartz (0001)

Earlier computational studies often relied on idealized, static surface terminations. Therefore, the pressure-dependent and temperature-dependent reconstructions were overlooked. These factors fundamentally govern the density of reactive sites available for catalysis. The α-quartz (0001) surface exhibits complex reconstruction behavior crucial for understanding the catalytic and interfacial properties of silica. Previous studies identified two principal low-energy reconstructions: a dense surface featuring a honeycomb arrangement of [SiO_4] tetrahedra (surface energy: 0.413 J/m^2) and a shifted surface with symmetry-breaking displacements of 3-member rings along the b-axis (0.404 J/m^2).[41] While Chen and colleagues first predicted these displacement reconstructions theoretically,[42] experimental verification came from Eder *et al.* using low-energy electron diffraction (LEED), revealing nanoscale twinning patterns.[43]

To systematically explore this complex configurational space, we performed sampling and training using HES-ML. During enhanced sampling, we discovered that constraining CV_{height} through the potential described in Eq. (5) (Sec. II) effectively promotes reconstruction (AIMD: CV_{height} = 8.6–9.4 Å; HyGSI-X: CV_{height} = 8.2–9.8 Å with 0.2 Å increments). Simulation temperatures varied from 300 to 1500 K (600 K increments for AIMD, 300 K for HyGSI-X), balancing thermal activation with controlled Si–O rebonding. Through this constraint-enhanced strategy, our AIMD simulations revealed three distinct surface configurations [Fig. 5(a)]: the A-type (dense surface), a previously unreported AB-type hybrid, and the B-type (shifted surface). The systematic application of pressure [Fig. 2(b), Eq. (S3)] enabled efficient exploration of surface reconstructions, overcoming limitations encountered by traditional approaches (such as ReaxFF$^{GSI}_{SiO}$) in navigating the vast parameter space of SiO_2 surface chemistry.

Comparative simulations using ReaxFF$^{GSI}_{SiO}$, BKS, and DeePMD potentials reveal notable differences in reconstruction behavior (Figs. S1–S3). The pre-paired oxygen–silicon average atomic distance ($\overline{D}_{O\text{-}Si}$) refers to specific O–Si pairs that form bonds upon reconstruction; thus, examining $\overline{D}_{O\text{-}Si}$ serves as a diagnostic for reconstruction occurrence and extent. DeePMD exhibited $\overline{D}_{O\text{-}Si}$ distributions spanning 1.55–3.5 Å, indicating relatively thorough exploration of both reconstructed and unreconstructed configurational spaces. By contrast, BKS showed distributions between 1.55 and 3.0 Å but lacked exploration beyond 2.8 Å, while ReaxFF$^{GSI}_{SiO}$ only achieved distributions above 2.6 Å, demonstrating its inability to achieve effective bonding reconstructions.

Further analysis provided detailed characterization of reconstruction capabilities under the temperature and pressure perturbations for ReaxFF$^{GSI}_{SiO}$, BKS, and DeePMD. ReaxFF$^{GSI}_{SiO}$ fails to reproduce surface reconstruction across all temperature-pressure conditions [Fig. 5(b)]. Si–O distances remain above 2.6 Å, indicating persistent repulsion rather than bonding rearrangement, consistent with its inability to access bonding-distance regions in the $\overline{D}_{O\text{-}Si}$ distribution. BKS achieved pressure-driven reconstructions with reasonable Si–O bonding distances (<3.0 Å at 1500 K), successfully reproducing all three AIMD-identified reconstruction types [Fig. 5(c)]. The phase diagram shows A-type dominance at low-to-intermediate temperatures (300–1300 K) and higher pressures (8.2–8.8 Å), while B-type prevails under low-temperature with intermediate-pressure or high-temperature with intermediate-to-high-pressure conditions. DeePMD demonstrated superior flexibility, with Si–O bond lengths spanning 1.55–>3.5 Å, capturing both low-temperature reconstruction accuracy and high-temperature stability [Fig. 5(d)]. The reconstruction phase diagram exhibits a dispersed, interleaved distribution-reflecting competing entropic and enthalpic effects under pressure–temperature perturbations. Notably, A-type reconstructions in DeePMD span broader temperature (300–1500 K) and pressure (8.2–9.1 Å) ranges, confirming their thermodynamic preference under high-pressure/low-temperature conditions, qualitatively consistent with previously

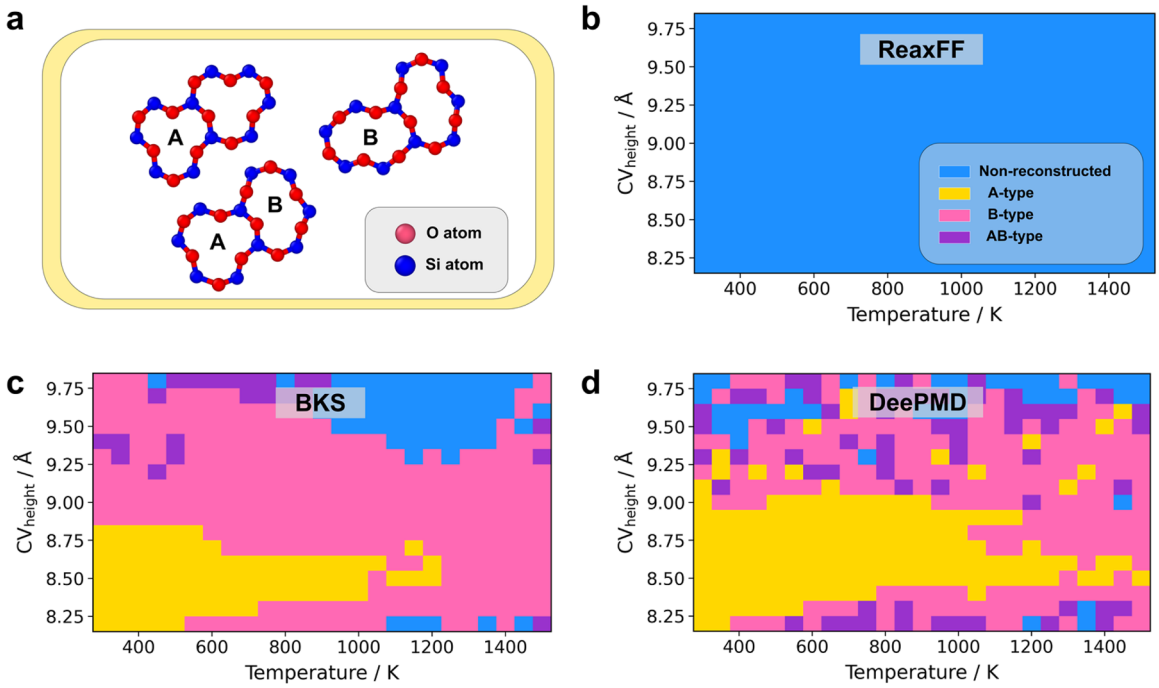

FIG. 5. Pressure-induced surface reconstructions of α-quartz (0001). [(a)–(c)] Reconstruction distribution maps showing reconstruction-type distributions as functions of CV_{height} (8.2–9.8, 0.2 Å increments) and temperature (300–1500, 300 K increments) for DeePMD (a), BKS (b), and $ReaxFF^{GSI}_{SiO}$ (c). For all three potentials, identical constraint-enhanced sampling protocols (same CV_{height} definition, cubic upper-wall restraint κ = 1000 kJ/mol, temperature–CV_{height} grid, and simulation time per condition) were applied, so the comparison isolates potential-energy-surface differences rather than sampling differences. The quantitative structural metrics of the three reconstruction types and their DFT single-point validation are given in Table S1. (d) Atomic configurations of surface reconstructions identified through constraint-enhanced AIMD: A-type, B-type, and AB-type.

calculated surface energy hierarchies (A-type: 0.413 J/m^2; B-type: 0.404 J/m^2).

These findings establish a reconstruction stability hierarchy consistent with surface energy calculations while revealing new insights: (1) AB-type exhibits high-temperature stability characteristics similar to B-type; (2) at fixed temperatures, higher instantaneous pressures favor dense A-type formation, while lower pressures promote relaxed B-type/AB-type displacements; (3) A-type displays deterministic formation patterns, contrasting with the stochastic distributions of B-type/AB-type, indicating entropic regulation. Pressure and temperature select between competing surface terminations. This reshapes the density and type of catalytic sites available for oxygen adsorption. Classical force fields fail to reproduce this coupling between structural evolution and reaction chemistry.

C. Oxygen adsorption based on HyGSI

Oxygen adsorption on reconstructed silica surfaces constitutes the fundamental steps for subsequent chemical processes, including oxidation, catalytic recombination, and ablation. Simulating this process faces dual challenges: system complexity and extensive thermodynamic sampling requirements. Traditional MD models, particularly the continuous atom injection/removal approach employed by Norman *et al.*[44] with $ReaxFF^{GSI}_{SiO}$, successfully determined catalytic recombination coefficients. However, the substantial energy fluctuations induced by continuous atom addition/removal, when coupled with NVT temperature control, obscure meaningful interfacial energy patterns, challenging adsorption process investigations. Moreover, the reliability of force fields raises fundamental questions regarding simulation fidelity.

Built upon HyGSI, we implement a two-stage computational protocol that addresses these challenges through strategic integration of complementary methods. The initial GCMC/RMD stage leverages the thermodynamic rigor of grand canonical ensemble sampling to explore accessible coverage spaces at each temperature–pressure condition. A notable feature of this protocol is a spatial partitioning scheme [Fig. 6(a)] that confines stochastic insertion and deletion operations to a narrow region above the surface. In addition, a soft potential [Eq. (S4)] applied to GCMC-inserted oxygen atoms prevents O_2 molecule formation, which would otherwise dominate ensemble statistics and mask surface chemistry. Three-stage temporal adaptation of GCMC parameters—progressing from aggressive initial sampling to conservative equilibrium collection—ensures both computational efficiency and sampling quality, revealing metastable configurations inaccessible to conventional molecular dynamics.

The subsequent RMD relaxation stage [Fig. 6(b)] transforms these thermodynamically sampled structures into fully optimized configurations by eliminating kinetic artifacts inherent to GCMC

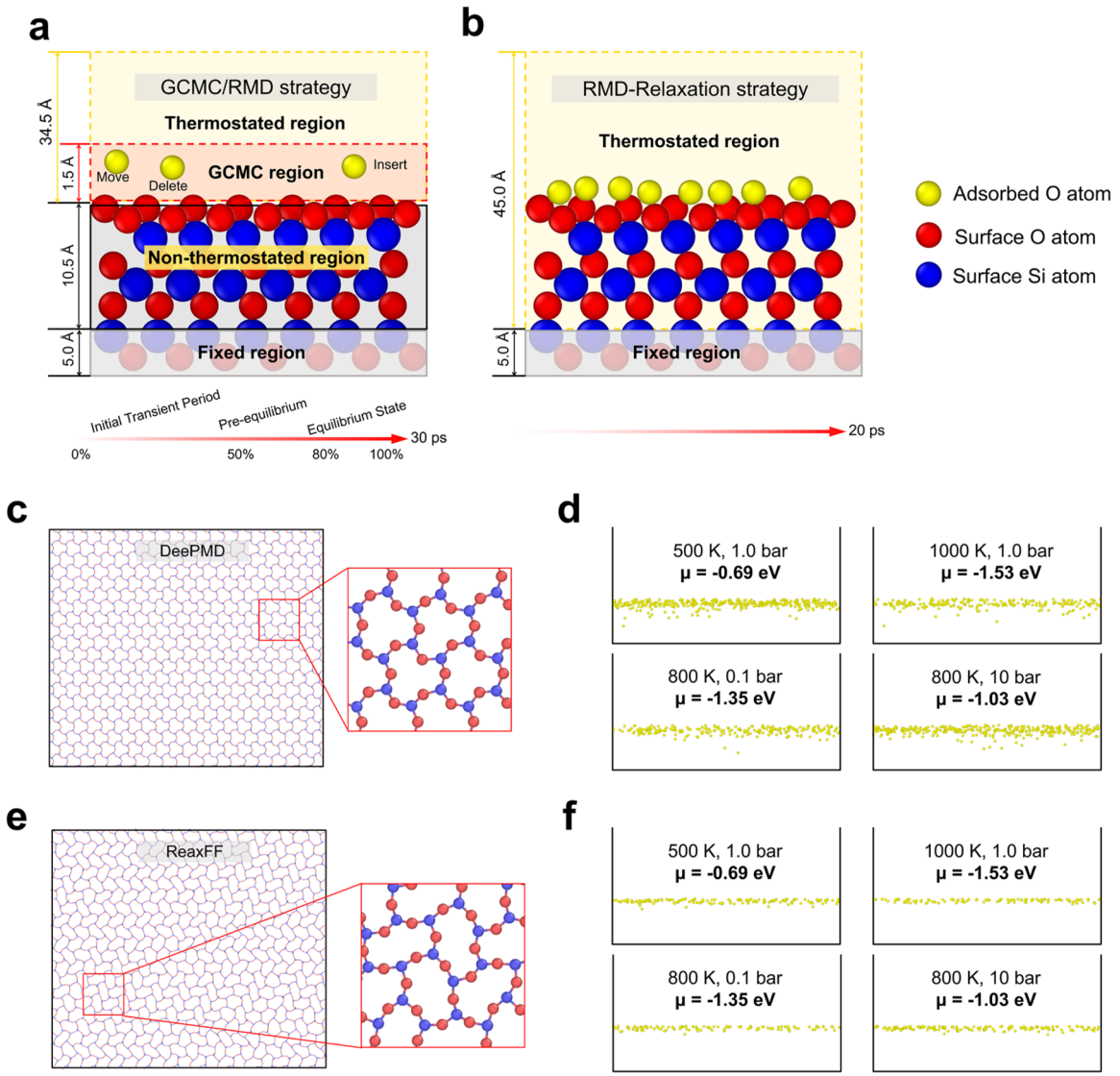

FIG. 6. Simulation framework and structural characterization of oxygen adsorption on SiO_2 surfaces. [(a) and (b)] Computational workflow: GCMC/RMD strategy for extensive thermodynamic sampling (a) and RMD-relaxation protocol for structural refinement and precise energy determination (b). [(c) and (d)] DeePMD results: Representative surface reconstruction modes upon adsorption (c) and snapshots of oxygen coverage with corresponding chemical potential (μ) evolution under varying temperature and pressure (d). [(e) and (f)] $ReaxFF^{GSI}_{SiO}$ results: Corresponding surface reconstruction modes (e) and coverage snapshots with μ evolution (f). Atom coloring: Si (blue), surface O (red), adsorbed O (yellow).

processes. By excluding auxiliary soft potentials employed during GCMC operations and implementing rigorous criteria for surface-bound species, this refinement yields adsorption energies and coverages that accurately reflect the underlying DeePMD potential. Continuous monitoring and removal of desorbed atoms ensures that computed properties correspond exclusively to chemisorbed oxygen. See the supplementary material for details.

This integration of surface reconstruction with adsorption dynamics differs significantly from previous work. We move beyond artificially cleaved surfaces to capture thermodynamically preferred structures. These structures dictate the actual adsorption site distributions at each specified temperature and pressure. Critically, we employed reconstructed structures as detailed in Methods: both DeePMD and $ReaxFF^{GSI}_{SiO}$ simulations utilized the dense A-type configuration obtained from HyGSI at 500 K. Following 10 ps relaxation at different temperatures (500–1000 K in 100 K intervals), surface reconstructions for DeePMD and $ReaxFF^{GSI}_{SiO}$ are shown in Figs. 6(c) and 6(e), respectively. DeePMD effectively maintains the A-type reconstruction, whereas $ReaxFF^{GSI}_{SiO}$ only sustains the looser B-type structure. As previously noted, although

$ReaxFF^{GSI}_{SiO}$ cannot spontaneously generate reconstructed surfaces under pressure–temperature induction, it maintains relative stability for pre-reconstructed structures-rationalizing Ye *et al.*'s catalytic recombination coefficient studies on reconstructed surfaces.[45] Nevertheless, $ReaxFF^{GSI}_{SiO}$ exhibits quantitative inaccuracies compared to DeePMD.

For the adsorption process, 54 thermodynamic state points per batch (0.1, 0.25, 0.5, 0.75, 1.0, 2.5, 5.0, 7.5, 10.0 atm across six temperatures, 500–1000 K in 100 K intervals) were computed across five parallel batches, yielding a total of 270 thermodynamic states. Comparing Figs. 6(d) and 6(f) reveals that GCMC chemical potential μ responds to both temperature and pressure, thereby modulating oxygen coverage and generating diversely distributed thermodynamic data. Notably, DeePMD produces oxygen coverages exceeding twice those of $ReaxFF^{GSI}_{SiO}$ under identical conditions, indirectly reflecting the latter's excessively high adsorption energies and the insensitivity of adsorption outcomes to μ variations. The sensitivity of the reported energetics to the GCMC soft-potential parameters, the insertion window, and the desorption–removal criterion was verified by a 40-run sensitivity study (≤±0.4 eV; Sec. IX and Fig. S5 of the supplementary material). The adsorption-energy definition, including the reference states, sign convention, and averaging protocol, is detailed in Sec. VIII of the supplementary material.

For the DeePMD surface adsorption results [Fig. 7(a)], the average coverages of the five datasets range from 2.1 to 5.1 atoms/nm,^{2} exhibiting logarithmic growth with inverse temperature. Higher pressures yield elevated coverages with diminished growth rates. Conversely, the average adsorption energies decrease logarithmically with inverse temperature; higher pressures produce larger adsorption energies with accelerated reduction rates. Pooled over all 270 state points [Fig. 7(c)], the adsorption energy shows no significant coverage dependence: the coverage-binned means remain flat at 2.90–3.00 eV from 2.4 to 4.7 atoms/nm^2, with a weak positive slope of only 0.1–0.2 eV per atom/nm^2 resolved at fixed temperature; $ReaxFF^{GSI}_{SiO}$, in contrast, exhibits a strong coverage dependence of −12.8 eV per atom/nm^2. The near invariance originates from the reconstructed-surface site lattice, whose median nearest-neighbor O_{ads}–O_{ads} spacing (~3.3 Å) exceeds the lateral interaction range between chemisorbed oxygens. The pooled mean is 2.96 eV; the quoted ±0.15 eV is the ensemble spread across all 270 state-point values, dominated by genuine condition-to-condition variation (0.12 eV), while the statistical uncertainty of the mean is below 0.01 eV (convergence protocol, block-averaging analysis, and

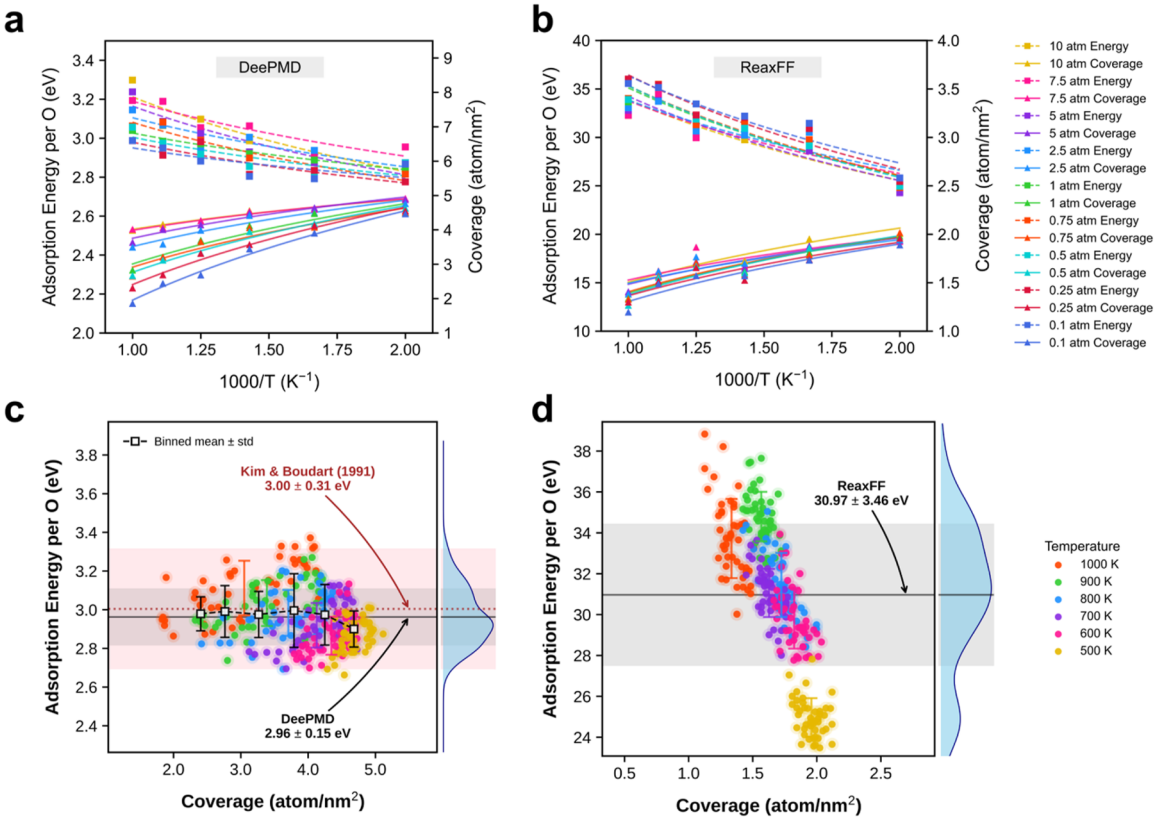

FIG. 7. Comparative energetics of oxygen adsorption on SiO_2 surfaces. [(a) and (c)] DeePMD adsorption thermodynamics: adsorption energy and surface coverage as a function of inverse temperature (a), and the distribution of adsorption energies vs coverage (c). [(b) and (d)] $ReaxFF^{GSI}_{SiO}$ adsorption thermodynamics: Corresponding analysis showing the temperature dependence of adsorption energy and coverage (b), and energy distribution profiles (d).

60 ps extended-relaxation validation are documented in Sec. X of the supplementary material). A single-point functional-sensitivity test at the hybrid PBE0-D3 level further bounds the DFT-level uncertainty of this value to ~±0.5 eV (Table S6). This value is consistent with the 1991 experimental estimate of 3.00 ± 0.31 eV by Kim and Boudart, who derived it from catalytic recombination experiments using the Hirschfelder relation.[42,43]

By contrast [Figs. 7(b) and 7(d)], although ReaxFF$^{GSI}_{SiO}$ captures qualitatively similar trends, including coverage variation with inverse temperature, pressure–coverage–value and growth rate relationships, and adsorption energy–temperature dependencies, quantitative discrepancies are substantial. ReaxFF$^{GSI}_{SiO}$ produces not only lower, narrower coverage distributions (1.1–2.1 atoms/nm^2) but also higher, broader adsorption energy distributions (30.97 ± 3.46 eV), approximately tenfold higher than the experimental values. This implies more difficult desorption reactions, less accurate catalytic recombination energy profiles, and consequently unreliable catalytic recombination coefficient statistics.

The validated adsorption energy indicates that each oxygen atom releases ~3 eV upon adsorption to SiO_2 surfaces. This adsorption-induced heating directly elevates surface temperature, providing a stable, continuous heat source to thermal protection materials regardless of subsequent catalytic O_2 recombination or surface ablation pathways. Given the strongly non-equilibrium nature of atmospheric re-entry, adsorption processes occur at the forefront of these phenomena. While alternative Si/O ReaxFF parameterizations differ quantitatively in their predicted adsorption energetics, the specific O/SiO_2 parameterization used here exhibits a ~10-fold overestimation (DeePMD: 2.96 ± 0.15 eV vs ReaxFF$^{GSI}_{SiO}$: 30.97 ± 3.46 eV). Although this order-of-magnitude discrepancy should not be generalized to all ReaxFF sets, systematic overbinding of atomic oxygen on silica is a documented tendency of charge-equilibration-based reactive force fields. The corrected adsorption energetics, thus, provides substantially revised input to heat-flux and catalytic-recombination models for atmospheric re-entry; direct heat-flux or TPS-sizing calculations are beyond the scope of this work and are left to future DSMC/CFD coupling studies. Future work should also extend the framework to full reaction networks via transition state theory.

IV. CONCLUSIONS

The oxygen adsorption energy on silica is 2.96 ± 0.15 eV, consistent with experiment but an order of magnitude lower than ReaxFF$^{GSI}_{SiO}$ predictions (~31 eV). This correction provides quantitatively revised energetics for atmospheric re-entry heat-flux models, rectifying previous overestimations of adsorption-induced thermal loads (~3 eV per impinging atom) caused by excessive ReaxFF binding energies. Beyond corrected energetics, HyGSI reveals that pressure and temperature select between competing surface terminations (A-type, B-type, AB-type), reshaping available catalytic sites—a coupling between structural evolution and reaction chemistry that classical force fields fail to reproduce. Furthermore, the adsorption energy is nearly coverage-invariant across the sampled range, consistent with Boudart's 1991 experimental inference, suggesting that surface saturation effects may limit catalytic efficiency at high oxygen flux, an effect future thermal-protection modeling may incorporate.

The HES-ML framework addresses a practical computational chemistry challenge: generating representative training data for rare events under extreme conditions. The iterative refinement between OPES-driven exploration and DeePMD training captures non-equilibrium configurations that conventional AIMD sampling misses. Current implementation requires expert-guided collective variable selection. Future work should extend the framework to other oxide surfaces (e.g., TiO_2, Al_2O_3) and incorporate additional collective variables for multi-step reaction networks.

HyGSI reproduces experimental adsorption energies, thermal expansion trends, and surface reconstruction patterns within a single potential. It provides a validated framework for modeling gas-surface chemistry under conditions inaccessible to experiments: temperatures and pressures where first-principles methods cannot reach equilibration timescales and classical force fields introduce systematic errors. The framework is applicable to other oxide surfaces where analogous accuracy–efficiency gaps exist, such as plasma–wall interactions in fusion reactors and catalytic oxidation on TiO_2.

SUPPLEMENTARY MATERIAL

The supplementary material provides detailed formulations of 3DSF and CVheight, supplementary figures of O–Si distance distributions, DeePMD model training details and datasets, and the full methodology for the hybrid GCMC/RMD and RMD-Relaxation strategy.

ACKNOWLEDGMENTS

This work was supported by the Strategic Priority Research Program of the Chinese Academy of Sciences (Grant No. XDA0380602). This work was supported by Beijing Super Cloud Computing Co., Ltd. through the provision of computational resources and technical assistance. We thank Zhiqi Shi (University of Chinese Academy of Sciences) for valuable contributions to this work. We are grateful to Yichong Chen, Yong Wang, and Zuoxu Li (Institute of Mechanics, Chinese Academy of Sciences) for insightful discussions.

AUTHOR DECLARATIONS

Conflict of Interest

The authors have no conflicts to disclose.

Author Contributions

Y.H. conceived the idea, designed the research, and supervised the overall project. G.Z. developed the HES-ML framework, performed AIMD and DFT calculations, conducted MD simulations, and carried out post-processing analyses. X.Y. constructed molecular models and performed MD simulations. S.H. assisted with AIMD, DFT, and MD simulations. Y.H. and G.Z. analyzed the data and interpreted the results. G.Z. wrote the original draft. T.X. and Y.Z. provided funding support and project oversight. Q.S. provided computational resources and high-level supervision. All authors discussed the results and contributed to the review and editing of the manuscript.

Guan Zhang: Conceptualization (equal); Data curation (equal); Formal analysis (equal); Funding acquisition (equal); Investigation (equal); Methodology (equal); Software (equal); Validation (equal); Visualization (equal); Writing – original draft (equal); Writing – review & editing (equal). **Xinbin Ye**: Conceptualization (equal); Formal analysis (equal); Methodology (equal); Software (equal). **Shiwei Hu**: Conceptualization (equal); Data curation (equal); Investigation (equal); Methodology (equal). **Yonghao Zhang**: Funding acquisition (equal); Investigation (equal); Resources (equal); Supervision (equal). **Tianbai Xiao**: Conceptualization (equal); Formal analysis (equal); Methodology (equal); Resources (equal); Supervision (equal); Writing – review & editing (equal). **Quanhua Sun**: Conceptualization (equal); Resources (equal); Supervision (equal). **Yuan Hu**: Conceptualization (equal); Data curation (equal); Investigation (equal); Project administration (equal); Resources (equal); Software (equal); Validation (equal); Writing – original draft (equal); Writing – review & editing (equal).

DATA AVAILABILITY

The training datasets and DeePMD models HyGSI are available at https://doi.org/10.5281/zenodo.18158696. The PLUMED input files, CP2k input files, and custom python scripts for data analysis and visualization are available at https://github.com/simplecellzg/HES-ML.git. The DeePMD-kit (v2.2.1) and PLUMED (v2.9.1) packages used are publicly available.

REFERENCES

[1] R. Knizikevičius, Vacuum **83**(6), 953–957 (2009).
[2] A. Kleyn, N. L. Cardozo, and U. Samm, Phys. Chem. Chem. Phys. **8**(15), 1761–1774 (2006).
[3] W. Guolin, Z. Yinjia, J. Hua, and M. Songhe, J. Exp. Fluid Mech. **33**(3), 13–19 (2019).
[4] L. He, Z. Cui, X. Sun, J. Zhao, and D. Wen, Nanomaterials **12**(14), 2370 (2022).
[5] L. Qin, Y. Xiaofeng, D. Wei, and D. Yanxia, Acta Aerodyn. Sin. **42**(4), 84–95 (2024).
[6] S. M. Davis, A. B. Belonoshko, B. Johansson, N. V. Skorodumova, and A. C. Van Duin, J. Chem. Phys. **129**(19), 194508 (2008).
[7] E. Iype, M. Hütter, A. P. J. Jansen, S. V. Nedea, and C. C. M. Rindt, J. Comput. Chem. **34**(13), 1143–1154 (2013).
[8] G. Shchygol, A. Yakovlev, T. Trnka, A. C. T. van Duin, and T. Verstraelen, J. Chem. Theory Comput. **15**(12), 6799–6812 (2019).
[9] H. Liu, X. Dong, and Y.-H. He, Acta Phys.-Chim. Sin. **30**(2), 232–240 (2014).
[10] T. T. Zhou, Y. D. Shi, and F. L. Huang, Acta Phys.-Chim. Sin. **28**(11), 2605–2615 (2012).
[11] O. R. Gittus and F. Bresme, J. Chem. Phys. **155**(11), 114501 (2021).
[12] X. Lu, X. Wang, Q. Li, X. Huang, S. Han, and G. Wang, Polym. Degrad. Stab. **114**, 72–80 (2015).
[13] J. Han, L. Zhang, and E. Weinan, Commun. Comput. Phys. **23**(3), 629–639 (2018).
[14] R. Car and M. Parrinello, Phys. Rev. Lett. **55**(22), 2471 (1985).
[15] C. Kim, M. Kim, S. Kim, M. Kang, M. S. Choi, and H. U. Kim, Adv. Electron. Mater. **10**, 2300835 (2024).
[16] W. Kohn and L. J. Sham, Phys. Rev. **140**(4A), A1133 (1965).
[17] G. Kresse and J. Furthmüller, Phys. Rev. B **54**(16), 11169 (1996).
[18] S. Lu, L. M. Ghiringhelli, C. Carbogno, J. Wang, and M. Scheffler, arXiv:2309.00195 (2023).
[19] Z. Xu and Y. Xia, J. Mater. Chem. A **10**(22), 11854–11880 (2022).
[20] G. M. Kanyolo and T. Masese, arXiv:2202.10323 (2022).
[21] D. Tolmachev, N. Lukasheva, R. Ramazanov, V. Nazarychev, N. Borzdun, I. Volgin, M. Andreeva, A. Glova, S. Melnikova, A. Dobrovskiy *et al.*, Int. J. Mol. Sci. **23**(2), 645 (2022).
[22] J. D. Herr and R. P. Steele, Chem. Phys. Lett. **661**, 42–47 (2016).
[23] M. Invernizzi and M. Parrinello, J. Chem. Theory Comput. **18**(6), 3988–3996 (2022).
[24] U. Raucci, V. Rizzi, and M. Parrinello, J. Phys. Chem. Lett. **13**(6), 1424–1430 (2022).
[25] P. Zhang, A. T. Gardini, X. Xu, and M. Parrinello, J. Chem. Inf. Model. **64**(9), 3599–3604 (2024).
[26] D. Ray, N. Ansari, V. Rizzi, M. Invernizzi, and M. Parrinello, J. Chem. Theory Comput. **18**(11), 6500–6509 (2022).
[27] S. Muscat, S. Errico, A. Danani, F. Chiti, and G. Grasso, J. Chem. Theory Comput. **20**(18), 8279–8289 (2024).
[28] A. D. Kulkarni, D. G. Truhlar, S. Goverapet Srinivasan, A. C. T. van Duin, P. Norman, and T. E. Schwartzentruber, J. Phys. Chem. C **117**(1), 258–269 (2013).
[29] T. Karmakar, M. Invernizzi, V. Rizzi, and M. Parrinello, Mol. Phys. **119**(19–20), e1893848 (2021).
[30] L. Bonati, V. Rizzi, and M. Parrinello, J. Phys. Chem. Lett. **11**(8), 2998–3004 (2020).
[31] M. Invernizzi, Nuovo Cim. C **44**, 112 (2021).
[32] A. C. T. van Duin, A. Strachan, S. Stewman, Q. Zhang, X. Xu, and W. A. Goddard, J. Phys. Chem. A **107**(19), 3803–3811 (2003).
[33] J. C. Fogarty, H. M. Aktulga, A. Y. Grama, A. C. Van Duin, and S. A. Pandit, J. Chem. Phys. **132**(17), 174704 (2010).
[34] J. Yeon and A. C. T. van Duin, J. Phys. Chem. C **120**(1), 305–317 (2016).
[35] T. D. Kühne, M. Iannuzzi, M. Del Ben, V. V. Rybkin, P. Seewald, F. Stein, T. Laino, R. Z. Khaliullin, O. Schütt, F. Schiffmann *et al.*, J. Chem. Phys. **152**(19), 194103 (2020).
[36] S. Grimme, WIREs Comput. Mol. Sci. **1**(2), 211–228 (2011).
[37] S. Grimme, J. Antony, S. Ehrlich, and H. Krieg, J. Chem. Phys. **132**(15), 154104 (2010).
[38] J. P. Perdew, K. Burke, and M. Ernzerhof, Phys. Rev. Lett. **77**(18), 3865 (1996).
[39] S. Goedecker, M. Teter, and J. Hutter, Phys. Rev. B **54**(3), 1703 (1996).
[40] J. VandeVondele and J. Hutter, J. Chem. Phys. **127**(11), 114105 (2007).
[41] O. D. Feya, Q. Wang, S. V. Lepeshkin, V. S. Baturin, Y. A. Uspenskii, and A. R. Oganov, Sci. Rep. **8**(1), 11947 (2018).
[42] Y.-W. Chen, C. Cao, and H.-P. Cheng, Appl. Phys. Lett. **93**(18), 181911 (2008).
[43] S. D. Eder, K. Fladischer, S. R. Yeandel, A. Lelarge, S. C. Parker, E. Søndergård, and B. Holst, Sci. Rep. **5**(1), 14545 (2015).
[44] P. Norman, T. E. Schwartzentruber, H. Leverentz, S. Luo, R. Meana-Pañeda, Y. Paukku, and D. G. Truhlar, J. Phys. Chem. C **117**(18), 9311–9321 (2013).
[45] X. Ye, S. Hu, G. Zhang, Y. Yan, Q. Sun, and Y. Hu, J. Phys. Chem. C **129**(1), 219–231 (2024).